# Uniaxial Néel vector control in perovskite oxide thin films by anisotropic strain engineering

K. Kjærnes [1], I. Hallsteinsen [1,2,*], R. V. Chopdekar [2], M. Moreau [1,4], T. Bolstad [1], I-H. Svenum [5,6]
S. M. Selbach [3], and T. Tybell [1,†]

[1]*Department of Electronic Systems, NTNU—Norwegian University of Science and Technology, 7491 Trondheim, Norway*
[2]*Advanced Light Source, Lawrence Berkeley National Laboratory, Berkeley, California 94720, USA*
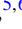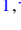[3]*Department of Materials Science and Engineering, NTNU—Norwegian University of Science and Technology, 7491 Trondheim, Norway*
[4]*Silicon Laboratories Norway AS, 0405 Oslo, Norway*
[5]*Department of Chemical Engineering, NTNU—Norwegian University of Science and Technology, 7491 Trondheim, Norway*
[6]*SINTEF Industry, 7034 Trondheim, Norway*

Antiferromagnetic (AF) thin films typically exhibit a multidomain state, and control of the AF Néel vector is challenging, as AF materials are robust to magnetic perturbations. In this paper, uniaxial Néel vector control is demonstrated by relying on anisotropic strain engineering of epitaxial thin films of the prototypical AF material LaFeO$_3$ (LFO). Orthorhombic (011)- and (101)-oriented DyScO$_3$, GdScO$_3$, and NdGaO$_3$ substrates are used to engineer different anisotropic in-plane strain states. The anisotropic in-plane strain stabilizes structurally monodomain monoclinic LFO thin films. The uniaxial Néel vector is found along the tensile strained $b$ axis, contrary to bulk LFO having the Néel vector along the shorter $a$ axis, and no magnetic domains are found. Hence, anisotropic strain engineering is a viable tool for designing unique functional responses, further enabling AF materials for mesoscopic device technology.

## I. INTRODUCTION

Antiferromagnetic (AF) materials have progressed over the past decade toward becoming an active rather than passive ingredient in energy-efficient spintronic devices [1–4]. AF materials are intrinsically spin compensated on the unit cell level, supporting a coherent spin structure essentially free of stray magnetic fields down to very small volumes. Moreover, AF materials display ultrafast dynamic responses, are nonvolatile, and can sustain spin currents over several micrometers [2,3,5]. Hence, AF materials possess several of the key features necessary for dense packing and ultrafast dynamics in memory applications. On the downside, however, AFs are exceedingly difficult to control by external magnetic fields, there is no straightforward way to control them by voltage, and they easily form magnetic domains [1]. Therefore, in commercial devices thus far, AFs have mainly been used as passive pinning layers for adjacent ferromagnetic materials via exchange bias.

For AF materials to take the active role, methods need to be found for engineering AFs with proper domain control supporting uniaxial spin structures at relevant length scales, which can be switched between stable states. With regard to switching, recent studies have shown that, in metallic AFs, it is possible to control AF domains using electric cur-

rents [6–10]. However, current-driven devices suffer from resistive Joule heating, and so insulating AFs could potentially enable spin transport without charge transport in energy-efficient spintronic devices [5,11–13]. In terms of AF domains, AF materials generally display domain formation, which affects spin transport [14]. To minimize domains with an unfavorable spin axis orientation thus remains an issue for taking full control of the spin texture and Néel vector over macroscopic as well as microscopic regions [15–17]. Strain engineering is an interesting tool in this regard, both for enhancement and tuning of functional properties [18]. It was recently predicted by density functional theory (DFT) calculations and demonstrated by use of piezoelectric strain that strain-mediated anisotropy can be used to control the Néel vector in manganese-based intermetallic AF systems [19,20]. Moreover, recent publications demonstrate strain control of the multiferroic domains in BiFeO$_3$ [21] and geometric strain-induced ferroelectricity in CaTiO$_3$ [22]. Also, structurally twin-free LaFeO$_3$ (LFO) films on GdScO$_3$ (GSO) were recently reported [23]. Nevertheless, the lack of AF domain control remains to be resolved.

The focus of this paper is on anisotropic strain engineering as a tool to control the spin structure through magnetocrystalline anisotropy. To this end, the prototypical AF insulator LFO is investigated. LFO exhibits the G-type AF structure with spin-polarized (111) planes and a high Néel temperature $T_N \approx 740$ K in bulk, the highest of all the orthoferrites [24–29]. The diamagnetic nature of La$^{3+}$ ensures magnetic stability for temperatures $< T_N$, and the orthorhombic structure (space group 62, *Pbnm*) provides structural stability up to $>1200$ K [30,31]. However, crystal twinning

---

*Present address: Department of Materials Science and Engineering, NTNU—Norwegian University of Science and Technology, Trondheim, Norway.
†Corresponding author: thomas.tybell@ntnu.no

is prevalent [32] due to LFO being ferroelastic [33,34], which makes it common to observe AF domains [35–39]. To take control of the AF domain structure, anisotropic strain engineering with highly distorted orthorhombic substrates is utilized for growth of monodomain LFO thin films. Two variants of the pseudocubic (111) facet found in orthorhombic systems are used to engineer different anisotropic in-plane strain states. In the cases where the in-plane strain anisotropy is large, as experienced by LFO, structurally monodomain thin films emerge where the magnetic response is consistent with an AF monodomain and uniaxial Néel vector. These findings enable engineering of AF systems with domain control and spin-axis orientation by design.

## II. METHODS

To investigate how anisotropic stain affects antiferromagnetism in LFO, epitaxial thin films were deposited on substrates of cubic and orthorhombic symmetry by pulsed laser deposition. The substrate temperature was $540\,°C$ and the substrate-target distance 45 mm for all samples, with a heater temperature ramp rate of $15\,°C\,min^{-1}$ for both heating and cooling. An oxygen background of 0.3 mbar was used during heating and deposition and 100 mbar during cooling. A KrF excimer laser ($\lambda = 248$ nm) with a fluence of $\sim2\,J\,cm^{-2}$ and 1–3 Hz repetition rate was used to ablate material from a sintered stoichiometric LFO target [40]. A series of pseudocubic (111)-oriented substrates were utilized: $DyScO_3$ (DSO), GSO, and $NdGaO_3$ (NGO), all orthorhombic (space group 62, *Pbnm*) [41,42], and isostructural to bulk LFO [32] and cubic $SrTiO_3$ (STO; space group 221, $Pm\bar{3}m$) [43]. The orthorhombic materials all possess the Glazer tilt pattern [44] $a^-a^-c^+$, and the distortion from ideal cubic perovskite is large in GSO and DSO, intermediate in NGO, and essentially zero in STO [41]. All substrates are commercially available and were received with standard surface miscut, typically $\pm0.3\,°$, from Shinkosha (Japan), SurfaceNet (Germany), and PI-KEM (England). Two orthorhombic substrate facets were used $(101)_o$ and $(011)_o$ corresponding to two distinct variants of the $(111)_{pc}$ facet, as illustrated in Fig. 1. The notation used to index a symmetry is from here on subscript c for cubic, r for rhombohedral, o for orthorhombic, m for monoclinic, t for triclinic, and pc for pseudocubic. The pseudocubic unit cell is defined in accordance with *Pbnm* notation, i.e., $[001]_{pc} \parallel [001]_o$ and $[110]_{pc} \parallel [100]_o$, resulting in $(101)_o$ and $(011)_o$ corresponding to $(111)_{pc}$ and $(\bar{1}11)_{pc}$, respectively. The upper row of Fig. 1 illustrates the response of the buckled hexagon of the $(111)_{pc}$ surface to the strain anisotropy of the two different orthorhombic facets. The two facets promote an opposite deformation relative to the pseudocubic axes, where $(101)_o$ and $(011)_o$ give relative elongation along $x = \langle 1\bar{1}0\rangle_{pc}$ and $y = \langle11\bar{2}\rangle_{pc}$, respectively. The lower row shows the two facets and how the pseudocubic unit cell relates to the orthorhombic unit cell with four formula units, i.e., $V_o \approx (\sqrt{2} \times \sqrt{2} \times 2)a_{pc}^3$, needed to correctly describe the distortions and octahedral rotations. The two facets are found by tilting the orthorhombic unit cell around the $a$ or $b$ axes, respectfully, as illustrated. Throughout the paper unit cell visualizations have been aided with VESTA 3 [45].
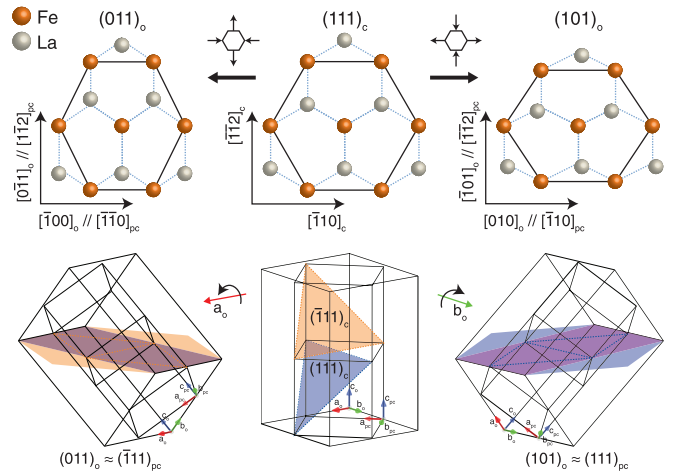


FIG. 1. Upper row: Orthorhombic equivalents of the cubic (111) plane and their effect on strain anisotropy along different crystallographic axes in the (111) pseudocubic plane. Upon going from the cubic symmetry to either of the two orthorhombic equivalents, one can note an opposite deformation of the buckled hexagons along the same pseudocubic directions. In addition, the orthorhombic symmetry accommodates an antipolar distortion of the A cations along the $b_o$ axis, which can be noted as successive shifts of La atoms up or down for $(011)_o$ and right or left for $(101)_o$. All distortions have been exaggerated for clarity. Lower row: The $(011)_o$ and $(101)_o$ orthorhombic planes (purple and pink shades) along with the respective $(111)_{pc}$ planes (orange and blue shades) shown together with the orthorhombic and cubic unit cells. The orthorhombic unit cell has approximately twice the height and four times the volume of a cubic unit cell.

A visual representation of the strain conditions investigated is shown in Fig. 2. The parameter $\zeta_{ab} = \frac{b_o-a_o}{a_o}$ is introduced as a measure of the degree of orthorhombic distortion in terms of relative difference between $a_o$ and $b_o$ axes. For cubic STO, it follows that $\zeta_{ab}$ is zero. The average pseudocubic strain is defined as $\varepsilon_{pc} = \frac{a_{pc(sub)}-a_{pc(film)}}{a_{pc(film)}}$, where $a_{pc} = \frac{\sqrt{a_o^2+b_o^2}+\frac{c_o}{2}}{3}$ is the pseudocubic parameter averaged over all three components of the orthorhombic unit cell. The anisotropic in-plane strain is defined by $\varepsilon_{x,y} = \frac{l_{x,y(sub)}-l_{x,y(film)}}{l_{x,y(film)}}$, where $l_x$ and $l_y$ are the length of the substrate or film unit cell along the $\langle1\bar{1}0\rangle_{pc}$ and $\langle11\bar{2}\rangle_{pc}$ directions, respectively (see Fig. 1). The series of substrates give access to an average strain range from $\varepsilon_{pc} = -1.72\%$ compressive strain in NGO to $\varepsilon_{pc} = +1.02\%$ tensile strain in GSO, for epitaxial LFO thin films. The strain depends strongly on in-plane crystal direction and substantially varies from the average strain. For example, for LFO on DSO$(101)_o$, along $[010]_o$, a tensile strain of 2.94% is expected, whereas along $[10\bar{1}]_o$, a compressive strain of 0.22% is expected. Moreover, it should be noted that, for a given substrate material, the two pseudocubic (111) facets $(011)_o$ and $(101)_o$ correspond to different in-plane strain values, albeit they have the same orthorhombic distortion. This is particularly well demonstrated for LFO on DSO and GSO, where the $(011)_o$ facet offers both substantial compression and elongation along the two principal in-plane axes, while the $(101)_o$ facet enables
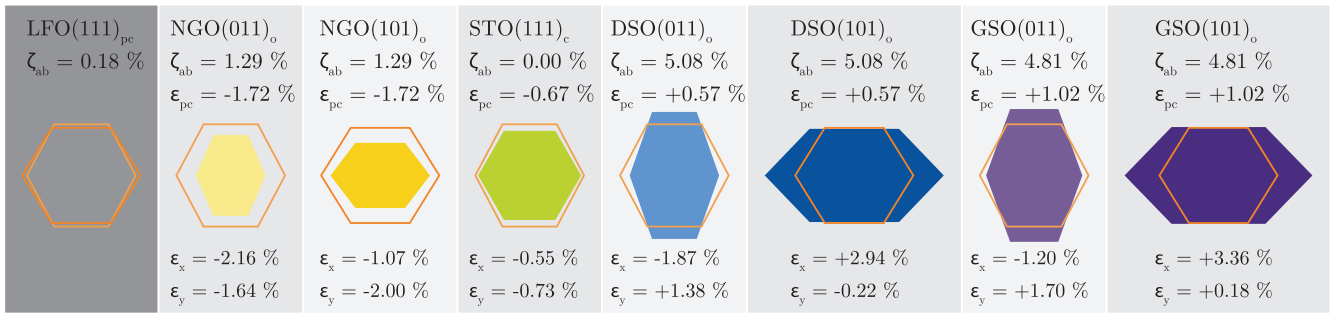
FIG. 2. Overview of strain conditions for LFO $(011)_o$ (light orange outline) and $(101)_o$ (orange outline) on all substrate facets (filled colors). The $(011)_o$ facet of LFO has been used for $STO(111)_c$. The figures are proportionally exaggerated to clearly convey the differences. Note that the level of orthorhombic distortion, denoted by $\zeta_{ab}$, is small in LFO, larger in NGO, and largest in the scandates.

a strong elongation along one direction and almost no strain along the other.

All substrates were surface-treated before deposition to ensure step-and-terrace surface quality. A standard cleaning routine with acetone and ethanol in an ultrasonic bath for 5 min each followed by drying under $N_2$ flow and annealing at 1000–1050 °C for 1–6 h was used for all substrates. Annealing was done in a closed furnace with pure $O_2$ flow, heating and cooling with 5 °C min$^{-1}$. $NGO(011)_o$ and $STO(111)_c$ were additionally etched in commercial grade hydrofluoric acid buffered in ammonium fluoride ($NH_4F : HF = 7 : 1$) for 30–60 s directly after cleaning and before annealing. *In situ* reflection high-energy electron diffraction data are consistent with initial two-dimensional layer-by-layer growth for deposition on all substrates [46]. Atomic force microscopy confirmed step-and-terrace topography of the grown samples with root mean square roughness typically < 500 pm.

Four-circle high resolution x-ray diffraction (XRD, Bruker D8 Discover) with Cu K-$\alpha_1$ radiation was used to characterize the crystalline quality and symmetry of the thin films. Approximately 17-nm-thick films were used in this paper to allow for a sufficiently large signal-to-noise ratio to determine the film symmetry by XRD. Rocking curves from the symmetric $(111)_{pc}$ reflections were used to assess growth quality, and full width at half maximum values were between 0.025 ° and 0.031 ° for all samples, of the same order as the substrates and consistent with high-quality thin films. The film thickness was confirmed by fitting the $\theta/2\theta$ data, and all samples exhibited clear thickness fringes, as shown in Fig. 3, indicating coherent growth. The data are plotted in order of decreasing substrate $(111)_{pc}$ lattice constant (increasing $2\theta$), and the two vertical lines indicate the bulk value for the $(011)_o$ and $(101)_o$ LFO facets. It is noted that the $NGO(101)_o$ is not phase pure, as the substrate shows a significant portion of $(011)_o$ domains. Also, LFO on $NGO(011)_o$ shows less thickness fringes and lower intensity, indicative of strain relaxation and domain formation. To determine crystal structure and strain state of the thin films, reciprocal space maps (RSMs) with linear scans in momentum space ($Q_z = Q_\perp$, $Q_{x,y} = Q_\parallel$) were used. The RSM data were collected from asymmetric reflections corresponding to pseudocubic (312), (132), (330), and (114) reflections as well as symmetric (222) reflections for all samples. Both grazing exit (+) and grazing incidence (−) geometries were utilized to account for limited signal intensity due to varying structure factors for some reflections used. It

is noted that grazing incidence geometry results in a larger Bragg signal from the thin film at the expense of additional diffuse scattering. The RSM data will be thoroughly presented and discussed later.
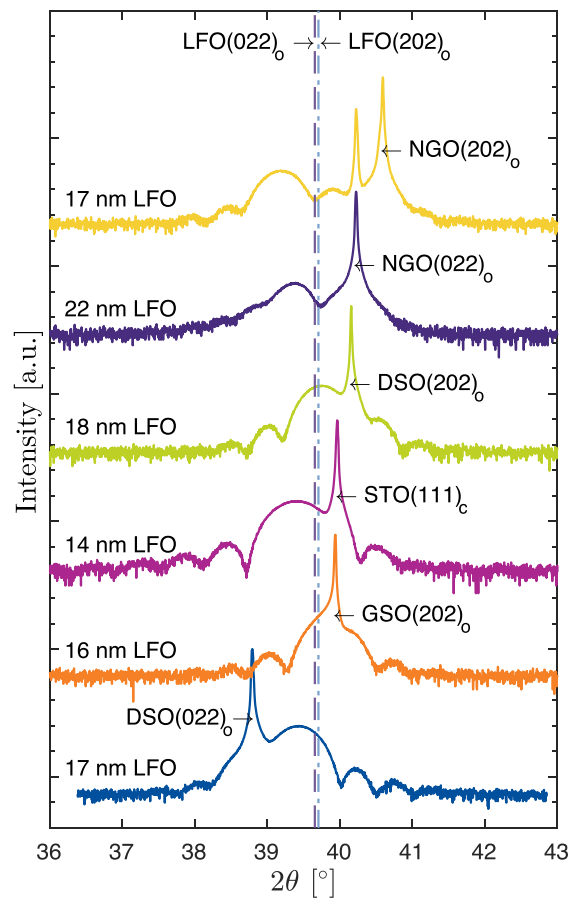


FIG. 3. Symmetric $\theta/2\theta$ scans for all samples offset for clarity. Each sample is labeled above the scan data on the left side, and the two vertical dashed lines represent the $(111)_{pc}$ planes of bulk LFO as labeled by the arrowed text on top. A straightforward relationship between substrate and film peak positions cannot be expected for $(111)_{pc}$ oriented interfaces, as the strain can be accommodated along directions other than the surface normal. Hence, there is not a monotonic shift of the LFO peak position when going from substrates with large $d_{(111)pc}$ for $DSO(011)_o$ toward decreasing $d_{(111)pc}$ for $NGO(101)_o$.

To corroborate the obtained crystal symmetries, the crystal structure of LFO under strain was also investigated by DFT calculations. The calculations were done with the Vienna *Ab initio* Simulation Package (VASP) [47,48], employing the projector augmented wave method [48,49]. The La, Fe, and O pseudopotentials supplied with VASP were used, treating 11, 14, and 6 electrons as valence states, with plane waves expanded up to a cutoff energy of 550 eV. Exchange correlation was described with the Perdew-Burke-Ernzerhof generalized gradient approximation for solids [50]. A Hubbard $U$ correction following the Dudarev approach [51] was applied. For the Fe $3d$ states, $U = 3$ eV was used [52]. For La, a large $U$ value is required to minimize $f$ electrons in the conduction band [53]; here, $U = 8$ eV was used, the largest $U$ value maintaining $a_o < b_o$ for bulk LFO. To calculate the crystal structure for strain parallel to the $(111)_{pc}$ facets, the supercells are reorientations of the cubic or orthorhombic cells into $2(\sqrt{2} \times \sqrt{2} \times \sqrt{3})a_{pc}$ pseudohexagonal cells with 120 atoms. The in-plane **a** and **b** vectors of the supercells were fixed to be equal to the DFT-calculated bulk values of the substrate materials, while the out-of-plane **c** vector was allowed to relax [54]. Brillouin zone integration was done on a $\Gamma$-centered $3 \times 3 \times 3$ k-point mesh for the strained LFO supercells. The geometry was optimized until all forces on the ions were $< 0.001$ eV Å$^{-1}$. Each orthorhombic facet was initialized with four different settings for the LFO supercell: (1) $a^-a^-c^+$ with the atomic coordinates from bulk LFO, (2) $a^-a^-c^0$ with the atomic coordinates from bulk LFO and zero long-axis octahedral rotations, (3) $a^-a^-a^-$ with atomic coordinates from a rhombohedral unit cell, and (4) $a^-a^-c^+$ with atomic coordinates from the more distorted substrate unit cell of the corresponding facet. These initializations were chosen to explore possible LFO ground states under anisotropic in-plane strain. All calculations were initialized with collinear G-type AF order on the Fe sublattice of LFO.

To assess the AF Néel vector orientation of the strained LFO films, x-ray absorption spectroscopy (XAS) was performed on beamline 4.0.2 at the Advanced Light Source (ALS), Lawrence Berkeley National Lab, in total-electron-yield mode by monitoring the sample drain current. Linearly polarized light was utilized to probe the x-ray magnetic linear dichroism (XMLD), with the XMLD defined as the difference signal between $p$- and $s$-polarized x-rays. XAS spectra were collected from the $L_2$ and $L_3$ edges of Fe and averaged over four to six subsequent scans per polarization, and the magnetic spin axis is interpreted based on the detailed features of the $L_{2A}$ and $L_{2B}$ multiplet. The $L_{2A}$ peaks for $p$- and $s$-polarization were normalized, and the relative magnitude of $L_{2B}$ with respect to $L_{2A}$ was used for interpretation of the Néel vector alignment [55]. Figure 4(a) displays typical Fe $L_2$ and $L_3$ edge spectra and the dichroism signal, and the inserts show the $L_2$ edge (b) before and (c) after normalization of the $L_2$ edge multiplet. Normalization is done by adjusting the $L_2$ pre-edge to zero and the $L_{2A}$ edge to one. A polarization signal with relative $L_{2B}$ magnitude $> L_{2A}$ is considered more perpendicular to the spin axis, and a polarization signal with relative $L_{2B}$ magnitude $< L_{2A}$ showing a double peak feature at the $L_{2B}$ high energy tail is considered more parallel to the spin axis. This interpretation is based on previous studies of (111)-oriented LFO [39,55] and (La, Sr)FeO$_3$ (LSFO) [56–58], where renor-
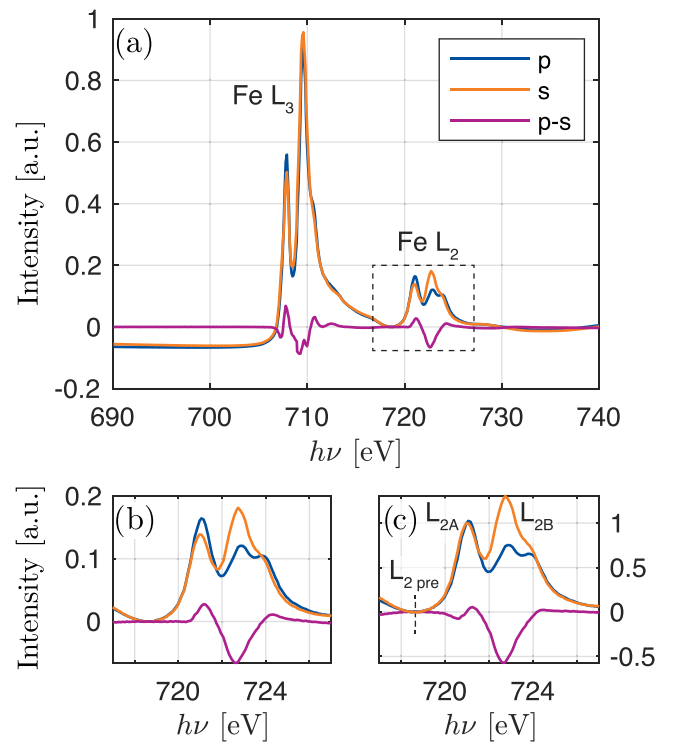


FIG. 4. (a) X-ray absorption spectra for $s$- and $p$-polarized x rays taken at the Fe $L_{2/3}$ edges. The x-ray magnetic linear dichroism (XMLD) effect is represented by the difference signal $p-s$ between polarizations. (b) Zoomed-in view of the $L_2$ multiplet with normalized data, and (c) zoomed in view of the $L_2$ multiplet after renormalization with the $L_2$ pre-edge set to zero and the $L_{2A}$ peaks set to one.

malization of the $L_2$ edge data gives $L_{2B}/L_{2A} \leqslant 0.9$ and $L_{2B}/L_{2A} \geqslant 1.3$ for relatively more parallel and perpendicular alignment, respectively. It is noted that a similar interpretation was used for (001)-oriented LFO [59] and LSFO [60], where the XMLD signatures were typical $I_0$ spectra for high-spin $d^5$ Fe$^{3+}$ ions in an octahedral crystal field [61,62]. The signature of a particular XMLD spectrum can most easily be recognized by the asymmetry shape at the $L_3$ edge [63]. The primary measurement geometry is shown in Fig. 5, where the incoming x rays have the in-plane projection along $[11\bar{2}]_{pc}$. In this geometry, $s$-polarization probes in plane along $[1\bar{1}0]_{pc}$ and $p$-polarization probes out of plane or in plane along $[11\bar{2}]_{pc}$ depending on the incidence angle $\theta$. The incidence angle was varied as $\theta \in [15°, \ 165°]$ with reference to the surface plane, where particularly $\theta = 35°$, $90°$, and $145°$ were used for all samples. This is illustrated in the bottom part of Fig. 5. At $\theta = 35°$, the photons are incident parallel to the substrate $c$ axis; hence, $p$- and $s$-polarization probe the orthorhombic $a$ and $b$ axes ($b$ and $a$ axes) for a thin film grown on the $(101)_o$ facet $[(011)_o$ facet], respectively. These axes represent the $[110]_{pc}$ and $[1\bar{1}0]_{pc}$ in the $ab$ plane. Probing along two axes belonging to the same $(hkl)$ family generally minimizes the influence of crystal field anisotropy effects on the XMLD spectra [57,61]; however, as evidenced by azimuthal data, the (111) facet appears to possess insignificant crystalline anisotropy in terms of influencing the XMLD effect [39,58]. By varying the incidence angle, the $p$-polarization gives good coverage of a Néel
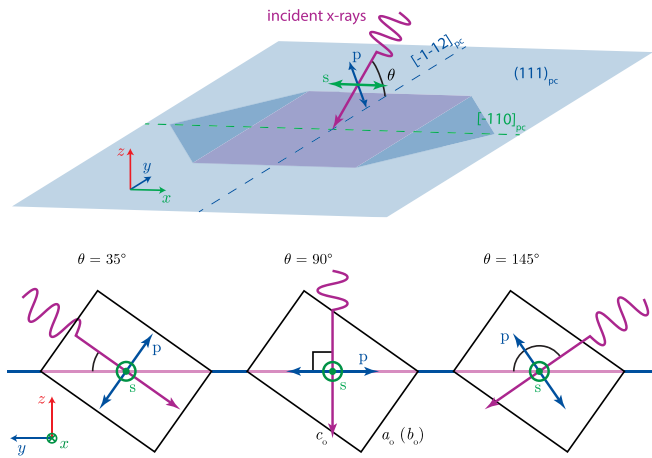
FIG. 5. Top: X-ray absorption spectroscopy (XAS) geometry for x-ray magnetic linear dichroism (XMLD) measurements. Incoming x rays are linearly polarized with either $s$- or $p$-polarization. Incidence angle varies with $\theta \in [15°, 165°]$, and the azimuthal direction is fixed to have the plane of incidence parallel to the $(1\bar{1}0)_{pc}$ symmetric plane and the $[11\bar{2}]_{pc}$ principal in-plane axis. The buckled hexagon $(111)_{pc}$ surface and the orthorhombic equivalent plane are indicated in blue and pink shades, respectively. The figures are made with reference to the $(101)_o$ orientation of the orthorhombic unit cell, and the coordinate system is defined as $\hat{x} \parallel [\bar{1}10]_{pc}$, $\hat{y} \parallel [\bar{1}\bar{1}2]_{pc}$, and $\hat{z} \parallel [111]_{pc}$. Bottom: The three most used incidence angles are drawn as seen along the $b_o$ ($a_o$) axis. Upon changing the incidence angle, $p$-polarization probes along different directions in the plane of incidence, while $s$-polarization stays fixed along $b_o$ ($a_o$).

vector component in the plane of incidence, without having to rotate the sample. It is noted that, despite the (111)-oriented geometry often enabling us to probe along $\langle 110 \rangle_{pc}$ or $\langle 111 \rangle_{pc}$ axes, the spectra measured here consistently correspond to $I_0$

signatures in accordance with previous studies on the (111) facet [39,52,55–58].

Furthermore, to investigate possible AF domain structure, x-ray photoemission electron microscopy (XPEEM) with linearly polarized light was done on the PEEM3 end station, beamline 11.0.1 at ALS. The XPEEM microscope has a fixed x-ray incidence angle of $\theta = 30°$ with reference to the sample surface, and the incident light was projected along the $[11\bar{2}]_{pc}$ direction with either $s$- or $p$-polarized light, like the XAS setup as seen in Fig. 5. The XMLD contrast at the Fe $L_2$ edge is calculated as defined for the XAS in a pixelwise manner in the field of view, to reveal contrast between areas which are to varying degrees magnetically aligned with the incident x-ray **E** vector.

## III. RESULTS AND DISCUSSION

### A. XRD data

First, the effect of anisotropic strain on the crystal structure of LFO is assessed. DFT data supporting the experimental findings, are presented and discussed in the Appendix. Figure 6 shows in panels (a) and (b) the crystal structure relations between rhombohedral (purple), orthorhombic (black), and monoclinic (orange) representations of a cubic (111) surface. Panel (c) presents the bulk orthorhombic crystal structure of LFO, whereas panel (d) depicts the LFO crystal structures inferred from this paper.

The RSM data for LFO on DSO(101)$_o$, DSO(011)$_o$, GSO(101)$_o$, NGO(101)$_o$, NGO(011)$_o$, and STO(111)$_c$ are given in Fig. 7. The axes are printed 1:1, i.e., the in-plane and out-of-plane components are to scale for all plots. Also note the dashed (dotted) horizontal line in each plot, hereby denoted the *symmetry line*, which corresponds to the out-of-plane values $Q_\perp$ for a system where all planes measured are
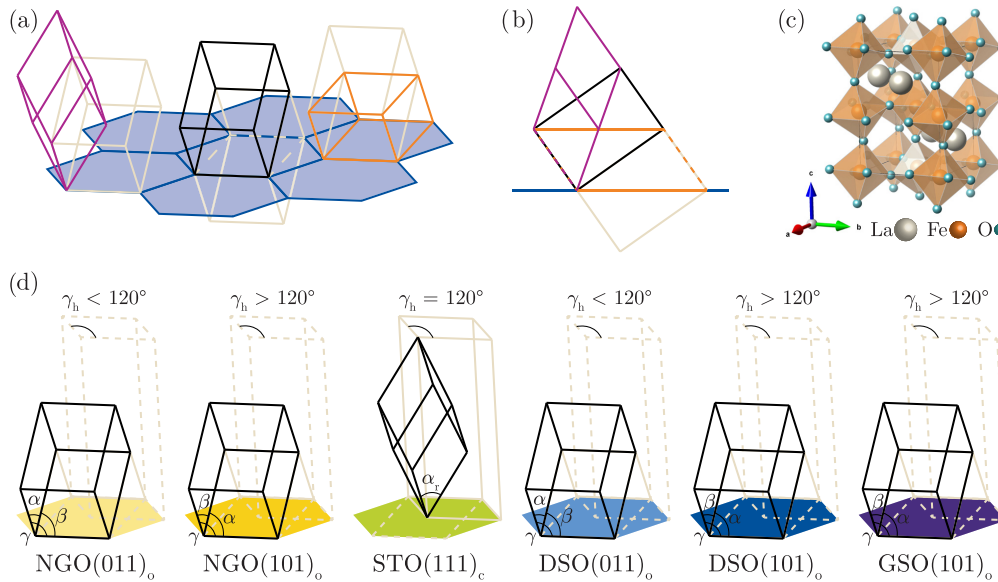


FIG. 6. Crystal structure relations on hexagonal symmetric (111) surfaces. (a) Rhombohedral (purple), orthorhombic (black), and monoclinic (orange) representations of a cubic (111) surface, and (b) profile view along $[1\bar{1}0]_{pc}$. (c) Bulk orthorhombic crystal structure of LFO. (d) Visual summary of the crystal structures found from this x-ray diffraction (XRD) study. The pseudo-orthorhombic representation is used for all films where a monoclinic or triclinic symmetry was found.
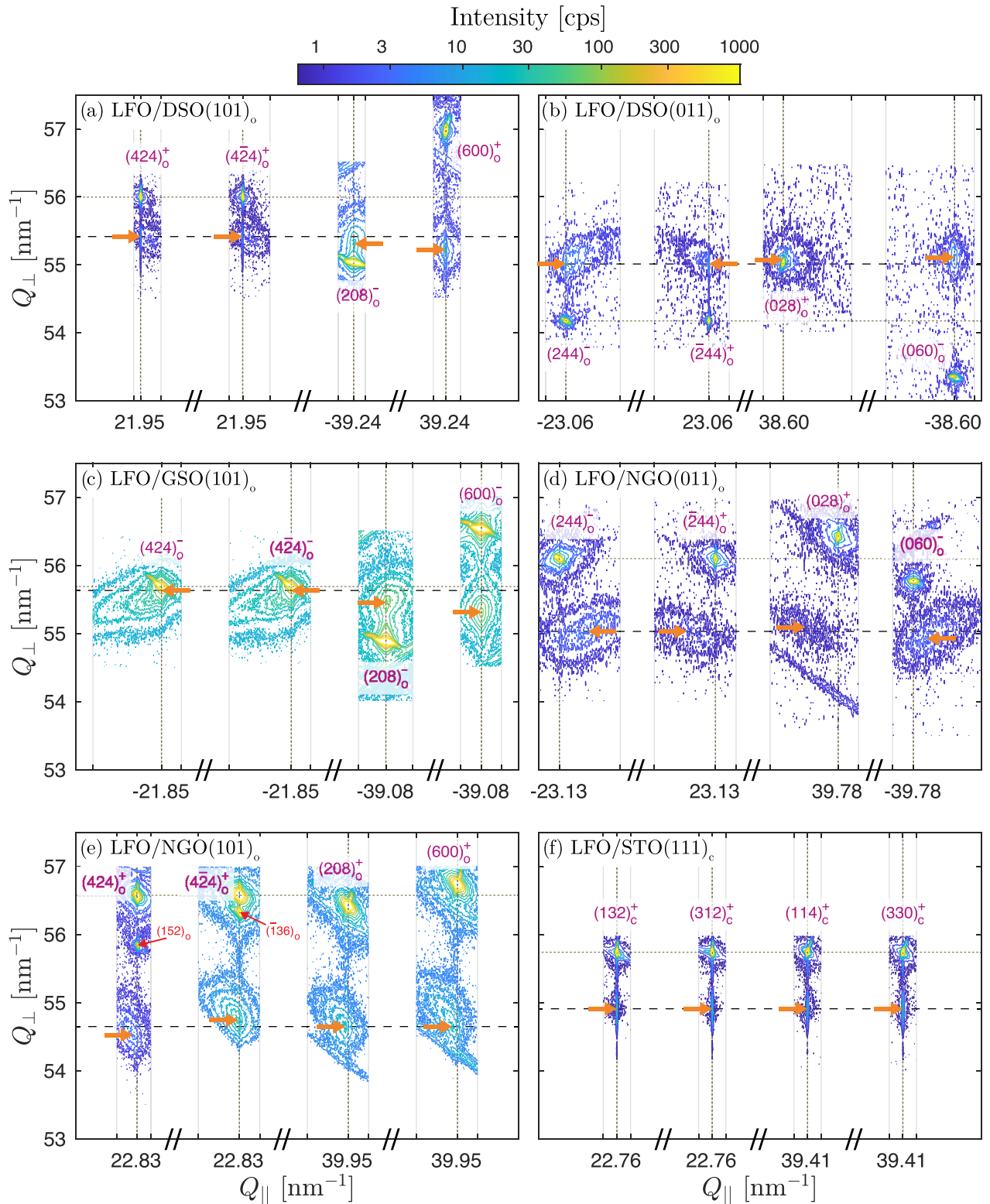
FIG. 7. Reciprocal space map (RSM) data for all samples. LFO on (a) DSO(101)$_o$, (b) DSO(011)$_o$, (c) GSO(101)$_o$, (d) NGO(011)$_o$, (e) NGO(101)$_o$, and (f) STO(111). Axes are 1:1, and all plots are to scale with one another for direct comparison. $x$-axis values and dotted vertical (horizontal) lines denote the substrate $Q_{||}$ (symmetric $Q_\perp$) for each reflection. Gray vertical lines show the in-plane limits of the RSM. The horizontal dashed lines are guides to the eye for comparison of the film reflection values $Q_\perp$. The film peaks are found at the orange arrowheads. The streaks that are seen around $Q_\perp \approx 54$ and $Q_\perp \approx 56.5$ in some of the high $Q_{||}$ scans have been verified to originate from the x-ray diffraction (XRD) system itself; they have nothing to do with the samples.

symmetric to its mirrored twin, i.e., a high-symmetry cubic or rhombohedral system. For the orthorhombic systems, an even asymmetry in $Q_\perp$ relative to the symmetry line comes from the fact that $a_{pc} = b_{pc} \neq c_{pc}$, which leads to a tilt of the pseudocubic unit cells so that $[111]_{pc}$ is no longer perfectly parallel to the surface normal. Orange arrows point toward the thin film peaks, either seen directly or inferred by partial relaxation or diffuse scattering.

In Fig. 7(a), RSM data for LFO on DSO(101)$_o$ are plotted. All LFO reflections have the same in-plane component $Q_\parallel$ as the substrate, consistent with coherent growth and epitaxial strain along both principal in-plane axes $[010]_o$ and $[10\bar{1}]_o$. The $(424)_o$ and $(4\bar{2}4)_o$ planes additionally show a broadened, weak signal at higher $Q_\parallel$, indicating an onset of partial relaxation. This can be rationalized due to a large tensile strain of 2.94% along this direction. The peak positions are symmetric in $Q_\perp$ for $(424)_o$ and $(4\bar{2}4)_o$, indicating no unit cell tilt along the $[010]_o$ ($[1\bar{1}0]_{pc}$) axis. From the $(208)_o$ and $(600)_o$ reflections, it is apparent that the film is slightly tilted along the $[10\bar{1}]_o$ ($[11\bar{2}]_{pc}$) axis, seen as a collective lowering and with different values in the out-of-plane components $Q_\perp$ with respect to the symmetry line. An asymmetry is expected in the $Q_\perp$ values for the $(208)_o$ and $(600)_o$ reflections due to the bulk orthorhombic unit cell, both for substrate and film. For the strained LFO to be orthorhombic, all the measured LFO $Q_\perp$ values would need to be identical to the substrate values, which is not the case. Thus, a reduction of symmetry to a monoclinic unit cell for LFO on DSO(101)$_o$ can be concluded, see Table I.

On DSO(011)$_o$, see Fig. 7(b), the results are like DSO(101)$_o$ but with a difference for the $(028)_o$ and $(060)_o$ reflections, where the out-of-plane $Q_\perp$ values for LFO are collectively increased from the symmetry line instead of decreased. The film peak is hidden by the substrate peak in the case for $(028)_o$, but by considering the diffuse scattering around the substrate peak, a film peak at slightly lower $Q_\perp$ than for $(060)_o$ is inferred. Hence, there is a small asymmetry in the opposing planes along the $[0\bar{1}1]_o$ ($[1\bar{1}2]_{pc}$) axis, and as DSO is orthorhombic, the in-plane anisotropy due to the epitaxial strain induces a lowering of LFO symmetry to monoclinic.

The situation for LFO on GSO(101)$_o$ is comparable with DSO(101)$_o$, see Fig. 7(c). The crystal symmetry is found to be monoclinic, but there is more partial relaxation than for LFO on DSO(101)$_o$ along the in-plane $[010]_o$ ($[1\bar{1}0]_{pc}$) axis, in agreement with an increased tensile strain to 3.11%. Note that, for the $(424)_o$ and $(4\bar{2}4)_o$ scans, the film reflections are partly hidden by the substrate; however, the film features were resolved using grazing incidence scans to increase film signal and diffuse contributions from nearby regions. The strained $Q_\perp$ values are inferred from relaxation lines following the diffuse scattering. Albeit partial relaxation is readily visible, RSM data for $(532)_o/(5\bar{3}2)_o$ and $(512)_o/(5\bar{1}2)_o$ (not shown) confirm the strained film along the in-plane $[010]_o$ ($[1\bar{1}0]_{pc}$) axis as well.

Next, the crystal symmetry of LFO on NGO is considered. LFO on NGO(011)$_o$, see Fig. 7(d), shows a less coherent and more relaxed film than any of the other cases. The $(244)_o$ and $(\bar{2}44)_o$ scans are symmetric both in and out of plane, and the $(028)_o$ and $(060)_o$ are asymmetric both in and out of plane.
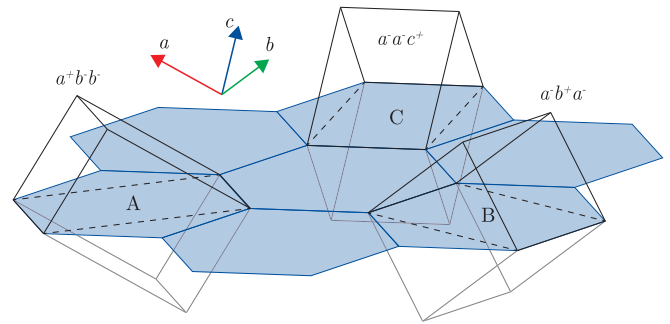


FIG. 8. The three structural domains an orthorhombic film material can take on a pseudocubic (111)-oriented surface. Arrows indicate the pseudocubic unit vectors, and the Glazer tilt system relative to these is stated for each structural domain. The domains are denoted A, B, and C, corresponding to the orientation of the long axis with in-phase octahedral rotations. If crystal twinning occurs, all three domains may have twins with a 90° rotation around the respective long axes ($a_o/b_o$ interchanged) to a total of six structural domains A, A′, B, B′, C, and C′.

The XRD data thus indicate structural domains present in the LFO film. The x-ray beam in this paper has a macroscopic footprint, about $0.4 \times 10$ mm$^2$ from the source monochromator, effectively making the diffracted signal a spatial average over multiple structural domains. In Fig. 8, the three structural domains an orthorhombic film can take on a (111)-oriented monodomain surface are shown. Each domain, A, B, or C, is distinguished by the long axis with in-phase octahedral rotations, which can be distributed among all three pseudocubic axes. In addition, each domain may occur with their 90° base-plane rotated twins, A′, B′, and C′, where the $a_o/b_o$ axes are swapped, resulting in up to six possible structural domains in total. However, upon increasing the distortion of the unit cell from ideal cubic through rhombohedral to orthorhombic, the likelihood of crystal twinning and structural domains is reduced. Returning to the LFO on NGO(011)$_o$ data, it thus appears that LFO is relaxed to the extent where it forms two or more structural domains. Based on the peak positions of the data, however, the symmetry of LFO reduces to monoclinic also in this case, and the average crystal structure is calculated based on these positions, see Table I.

For LFO on NGO(101)$_o$, Fig. 7(e), the picture is more complicated than for (101)$_o$ DSO and GSO. The film peaks are broadened in $Q_\parallel$, indicating domains, and some degree of relaxation toward bulk LFO values can be seen. In this case, the $\theta/2\theta$ scan for LFO on NGO(101)$_o$ (Fig. 3) reveals a significant contribution from (011)$_o$ domains in the substrate, and the $(424)_o$ and $(4\bar{2}4)_o$ scans show explicitly the signature of another domain in the substrate [Fig. 7(e) red arrows/labels]. This signature corresponds to (011)$_o$ domains oriented as $a^+b^-b^-$ (A′ domains, Fig. 8) with respect to the primary $a^-a^-c^+$ (101)$_o$ (C domain, Fig. 8). Thus, the additional substrate peaks seen in the RSM data correspond to reflections of $(152)_o$ and $(\bar{1}36)_o$, where the in-plane components are similar, whereas the out-of-plane components differ substantially, as compared with $(424)_o$. The (011)$_o$ domains are in this case oriented with the $[11\bar{1}]_o$ direction parallel to the main $[010]_o$ ($[1\bar{1}0]_{pc}$) axis. As for LFO on NGO(011)$_o$,

TABLE I. Complete overview of the crystal structure data found from RSM and DFT for LFO on all substrate facets. Data column describes experimental data from literature or RSM (Ref./Exp.), DFT data relaxed from literature data (Relax.), and DFT data for LFO strained to the respective facets with different LFO supercell initializations ($a^-a^-c^+$, $a^-a^-c^0$, $a^-a^-a^-$, $a^-a^-c^+$sw). The $a^-a^-c^+$sw initialization is based on the relaxed DFT cells for each substrate with La/Fe swapped for the respective A/B cations of the substrates. All data are presented on the same format following the orthorhombic orientation of the substrates. The symmetries are deduced from the supercells using FINDSYM [64,65]. *For STO, the LFO structure found from RSM has been given twice, in both rhombohedral and monoclinic symmetry, to facilitate easier comparison of data.

| System | Data | Sym. | Space group | $a$ [Å] | $b$ [Å] | $c$ [Å] | $\alpha$ [°] | $\beta$ [°] | $\gamma$ [°] | $V$ [Å³] | Glazer | $\Delta E$ [meV /f.u.] |
|---|---|---|---|---|---|---|---|---|---|---|---|---|
| Bulk LFO | Ref. [32] | O | 62-3 $Pbnm$ | 5.553 | 5.563 | 7.867 | 90 | 90 | 90 | 243.022 | $a^-a^-c^+$ | |
| | Relax. | O | 62-3 $Pbnm$ | 5.5595 | 5.5630 | 7.8458 | 90 | 90 | 90 | 242.6483 | $a^-a^-c^+$ | 0.0 |
| DSO(101)$_o$ | Exp. | M | 14-8 $P2_1/n$ | 5.57 | 5.73 | 7.83 | 90 | 90.04 | 90 | 249.52 | | |
| | $a^-a^-c^+$ | M | 14-8 $P2_1/n$ | 5.5271 | 5.6895 | 7.7837 | 90 | 89.8980 | 90 | 244.7690 | $a^-a^-c^+$ | +13.9 |
| | $a^-a^-c^0$ | M | 14-8 $P2_1/n$ | 5.5271 | 5.6895 | 7.7837 | 90 | 89.8985 | 90 | 244.7668 | $a^-a^-c^+$ | +13.9 |
| | $a^-a^-a^-$ | M | 15-3 $I2/a$ | 5.4929 | 5.6895 | 7.7781 | 90 | 90.2091 | 90 | 243.0750 | $a^-a^-c^0$ | +25.1 |
| | $a^-a^-c^+$sw | M | 14-8 $P2_1/n$ | 5.4396 | 5.6895 | 7.9057 | 90 | 89.2626 | 90 | 244.6485 | $a^-a^-c^+$ | +26.4 |
| DSO(011)$_o$ | Exp. | M | 14-7 $P2_1/b$ | 5.45 | 5.60 | 7.96 | 90.40 | 90 | 90 | 243.14 | | |
| | $a^-a^-c^+$ | M | 14-7 $P2_1/b$ | 5.3885 | 5.6278 | 7.9316 | 89.8292 | 90 | 90 | 240.5269 | $a^-a^-c^+$ | +34.9 |
| | $a^-a^-c^0$ | M | 14-7 $P2_1/b$ | 5.3885 | 5.6278 | 7.9316 | 89.8290 | 90 | 90 | 240.5277 | $a^-a^-c^+$ | +34.9 |
| | $a^-a^-a^-$ | M | 15-9 $I2/c$ | 5.3885 | 5.5720 | 7.9048 | 90.5098 | 90 | 90 | 237.3282 | $a^-a^-c^-$ | +66.8 |
| | $a^-a^-c^+$sw | M | 14-7 $P2_1/b$ | 5.3885 | 5.6831 | 7.8659 | 90.0935 | 90 | 90 | 240.8800 | $a^-a^-c^+$ | +38.4 |
| GSO(101)$_o$ | Exp. | M | 14-8 $P2_1/n$ | 5.57 | 5.75 | 7.83 | 90 | 90.50 | 90 | 250.63 | | |
| | $a^-a^-c^+$ | M | 14-8 $P2_1/n$ | 5.5213 | 5.7203 | 7.7966 | 90 | 90.3416 | 90 | 246.2379 | $a^-a^-c^+$ | +21.7 |
| | $a^-a^-c^0$ | M | 14-8 $P2_1/n$ | 5.5212 | 5.7203 | 7.7966 | 90 | 90.3424 | 90 | 246.2344 | $a^-a^-c^+$ | +21.7 |
| | $a^-a^-a^-$ | M | 15-3 $I2/a$ | 5.4819 | 5.7203 | 7.7876 | 90 | 90.7301 | 90 | 244.1817 | $a^-a^-c^{0(-\delta)}$ | +35.7 |
| | $a^-a^-c^+$sw | M | 14-8 $P2_1/n$ | 5.4450 | 5.7203 | 7.9013 | 90 | 89.8046 | 90 | 246.0997 | $a^-a^-c^+$ | +29.4 |
| GSO(011)$_o$ | $a^-a^-c^+$ | M | 14-7 $P2_1/b$ | 5.4315 | 5.6146 | 7.9367 | 90.3159 | 90 | 90 | 242.0286 | $a^-a^-c^+$ | +20.0 |
| | $a^-a^-c^0$ | M | 14-7 $P2_1/b$ | 5.4315 | 5.6146 | 7.9367 | 90.3153 | 90 | 90 | 242.0311 | $a^-a^-c^+$ | +20.0 |
| | $a^-a^-a^-$ | M | 15-9 $I2/c$ | 5.4315 | 5.5557 | 7.9079 | 91.0462 | 90 | 90 | 238.5889 | $a^-a^-c^-$ | +47.3 |
| | $a^-a^-c^+$sw | M | 14-7 $P2_1/b$ | 5.4315 | 5.6779 | 7.8613 | 90.6198 | 90 | 90 | 242.4272 | $a^-a^-c^+$ | +25.2 |
| NGO(101)$_o$ | Exp. | T | 2 $P$-1 | 5.57 | 5.52 | 7.81 | 89.74 | 88.26 | 89.64 | 239.84 | | |
| | $a^-a^-c^+$ | M | 14-8 $P2_1/n$ | 5.5658 | 5.5342 | 7.7596 | 90 | 88.2552 | 90 | 238.9002 | $a^-a^-c^+$ | +25.7 |
| | $a^-a^-c^0$ | M | 14-8 $P2_1/n$ | 5.5657 | 5.5342 | 7.7596 | 90 | 88.2557 | 90 | 238.8974 | $a^-a^-c^+$ | +25.7 |
| | $a^-a^-a^-$ | M | 15-3 $I2/a$ | 5.5529 | 5.5342 | 7.7688 | 90 | 88.2542 | 90 | 238.6269 | $a^-a^-a^-$ | +32.8 |
| | $a^-a^-c^+$sw | M | 14-8 $P2_1/n$ | 5.5405 | 5.5342 | 7.7955 | 90 | 88.0713 | 90 | 238.8908 | $a^-a^-c^+$ | +27.9 |
| NGO(011)$_o$ | Exp. | M | 14-7 $P2_1/b$ | 5.53 | 5.59 | 7.81 | 89.40 | 90 | 90 | 241.67 | | |
| | $a^-a^-c^+$ | M | 14-7 $P2_1/b$ | 5.4078 | 5.6081 | 7.8253 | 88.2094 | 90 | 90 | 237.2014 | $a^-a^-c^{+(-\delta)}$ | +56.4 |
| | $a^-a^-c^0$ | M | 14-7 $P2_1/b$ | 5.4078 | 5.6080 | 7.8252 | 88.2103 | 90 | 90 | 237.1972 | $a^-a^-c^{+(-\delta)}$ | +56.4 |
| | $a^-a^-a^-$ | M | 15-9 $I2/c$ | 5.4078 | 5.5928 | 7.8269 | 88.2998 | 90 | 90 | 236.6182 | $a^-a^-c^-$ | +71.2 |
| | $a^-a^-c^+$sw | M | 14-7 $P2_1/b$ | 5.4078 | 5.6446 | 7.7814 | 88.3895 | 90 | 90 | 237.4305 | $a^-a^-c^{+(-\delta)}$ | +58.0 |
| STO(111)$_c$ | Exp.* | R | 167-2 $R$-3$c$ | 5.58 | | | | 59.34 | | 120.88 | | |
| | Exp.* | M | 14-8 $P2_1/n$ | 5.58 | 5.52 | 7.85 | 90 | 89.19 | 90 | 241.77 | | |
| | $a^-a^-c^+$ | M | 14-8 $P2_1/n$ | 5.5739 | 5.5078 | 7.8361 | 90 | 89.0403 | 90 | 240.5332 | $a^-a^-c^+$ | – |
| Bulk DSO | Ref. [41] | O | 62-3 $Pbnm$ | 5.4494 | 5.7263 | 7.9132 | 90 | 90 | 90 | 246.9306 | $a^-a^-c^+$ | |
| | Relax. | O | 62-3 $Pbnm$ | 5.3885 | 5.6895 | 7.8706 | 90 | 90 | 90 | 241.2944 | $a^-a^-c^+$ | – |
| Bulk GSO | Ref. [41] | O | 62-3 $Pbnm$ | 5.4862 | 5.7499 | 7.9345 | 90 | 90 | 90 | 250.2946 | $a^-a^-c^+$ | |
| | Relax. | O | 62-3 $Pbnm$ | 5.4315 | 5.7203 | 7.8920 | 90 | 90 | 90 | 245.2026 | $a^-a^-c^+$ | – |
| Bulk NGO | Ref. [42] | O | 62-3 $Pbnm$ | 5.4332 | 5.5034 | 7.7155 | 90 | 90 | 90 | 230.7017 | $a^-a^-c^+$ | |
| | Relax. | O | 62-3 $Pbnm$ | 5.4078 | 5.5342 | 7.7017 | 90 | 90 | 90 | 230.4914 | $a^-a^-c^+$ | – |
| Bulk STO | Ref. [43] | C | 221 $Pm$-3$m$ | 3.9049 | | | | 90 | | 59.5429 | $a^0a^0a^0$ | |
| | Relax. | C | 221 $Pm$-3$m$ | 3.8946 | | | | 90 | | 59.0743 | $a^0a^0a^0$ | – |

the film peak positions are used for calculation of an average unit cell since the film thickness is not sufficient for the RSM data to resolve individual film domains. Interestingly, for LFO on NGO(101)$_o$, the RSM data show an asymmetry along in-plane $[010]_o$ ($[1\bar{1}0]_{pc}$) rather than $[10\bar{1}]_o$ ($[11\bar{2}]_{pc}$). This is seen as a splitting of $Q_\perp$ values for LFO peaks in $(424)_o$ and $(4\bar{2}4)_o$ scans relative to the symmetry line. The $(208)_o$ and $(600)_o$ LFO reflections instead fall on similar $Q_\perp$ values. This pattern is consistent with a lowering of LFO symmetry to triclinic due to the unit cell being tilted slightly toward $[010]_o$, indicating that $a_{pc} \neq b_{pc} \neq c_{pc}$ and $\alpha \neq \beta \neq \gamma \neq 90°$. Details for the unit cell refinement can be found in Table I.

Lastly, LFO on STO(111)$_c$ is included as a cubic system for reference where the substrate strain is isotropic. As seen in Fig. 7(f), all reflections have the same in-plane component

$Q_\parallel$ as the substrate, consistent with coherent growth and fully strained films along both principal in-plane axes $[1\bar{1}0]_{pc}$ and $[11\bar{2}]_{pc}$. The peak positions of $Q_\perp$ for all film reflections are constant, as is the case for the substrate reflections since STO is cubic. This implies no unit cell tilt along either of the principal in-plane axes $[1\bar{1}0]_{pc}$ and $[11\bar{2}]_{pc}$. Hence, the RSM data are consistent with a rhombohedral LFO unit cell, with a reduced rhombohedral angle of $\alpha_r = 59.34°$ from the ideal cubic value $\alpha_{r,\,STO} = 60°$, in accordance with an out-of-plane elongation in real space due to the compressive strain. This effectively yields an increase of symmetry in comparison with bulk LFO, indicating a polydomain film. However, DFT calculations for LFO on STO(111)$_c$, see the Appendix, reveal a monoclinic structure in agreement with a (101) pseudo-orthorhombic unit cell. This discrepancy between the monoclinic unit cell found by DFT calculations and rhombohedral by XRD can be explained by structural domains. LFO on STO(111)$_c$ is reported to exhibit three to six structural twins (Fig. 8) due to the symmetric biaxial strain [39,66,67], corresponding to a threefold rotation of the monoclinic unit cell found by DFT calculations. While the XRD signals are spatially averaging many of these, the film thicknesses here do not allow for separation of different domains. Indeed, by disregarding the octahedral rotations and antiferrodistortive A-cation shifts in the DFT results, i.e., neglecting the O and La atoms and considering only the high-symmetric Fe ion positions, the structure obtained from DFT calculations has rotational symmetry around the (111)$_{pc}$ normal. The unit cell is not tilted along either of the in-plane axes due to the symmetric STO strain. Thus, the calculated unit cell can support up to six structural variants on STO(111)$_c$ if $a/b$ twins are included, in agreement with the rhombohedral signature found by XRD.

As shown in the Appendix, DFT calculations of LFO on the various substrates agree well with the RSM results for the crystal structure of LFO thin films on all pseudocubic (111) substrate facets included, see the DFT data discussed and summarized in the Appendix and Table I. Importantly, the XRD RSM data indicate structurally monodomain samples when grown on the highly distorted orthorhombic substrates.

### B. XMLD data

The effect of anisotropic strain on the AF structure of LFO was investigated by XAS. For grazing incidence of $\theta = 35°$, $p$-polarized x rays have the **E** vector aligned with the bulk LFO Néel vector along the $a$ axis $[100]_o$, about 55° out-of-plane from the (111)$_{pc}$ surface, or the alternative in-plane $b$ axis $[010]_o$ for $s$-polarized x rays. Based on previous studies, it is expected to find the Néel vector along one of these axes [35,55,56], i.e., the $[110]_{pc}$ or $[\bar{1}10]_{pc}$ axes, respectively. Figure 9 shows the total electron yield signal for $s$- and $p$-polarization at incidence angles $\theta = 35°$, $90°$, and $145°$ for all samples. In the following, $\theta = 90°$ will correspond to normal incidence, and $\theta = 35°$ and $145°$ are denoted opposite grazing incidences. In this geometry, the spectra are measured with the plane of incidence parallel to the in-plane axes $[10\bar{1}]_o$, $[01\bar{1}]_o$, and $[11\bar{2}]_c$ for facets (101)$_o$, (011)$_o$, and (111)$_c$, respectively. For each sample, the $p$-polarization signal will change if the x-ray **E** vector becomes aligned with

the Néel vector as a function of incidence angle $\theta$, while the $s$-polarization signal should be constant with $\theta$, possibly varying slightly due to the footprint and penetration depth being dependent on incidence angle. The relative magnitudes of the $L_{2A/B}$ peaks are thus decisive for the interpretation of the Néel vector alignment.

First, the XMLD analysis of LFO with structural domains is presented. As previously reported, LFO on STO(111)$_c$ has a symmetric in-plane response with multiple AF domains aligned along the six in-plane $\langle 1\bar{1}0 \rangle_c$ and $\langle 11\bar{2} \rangle_c$ directions [39,55,66], consistent with the above-discussed XRD analysis, showing an effective rhombohedral unit cell due to averaging over different monoclinic twin domains oriented along the three degenerate $\langle 1\bar{1}0 \rangle_c$ directions. Particularly, Hallsteinsen $et~al.$ [39] found no dichroism between $p$- and $s$-polarization in normal incidence, whereas grazing incidence data exhibited clear dichroism independent of azimuthal rotation. Hence, the AF domain projections onto the polarization vector are evenly distributed along the two perpendicular in-plane axes $[1\bar{1}0]_c$ and $[11\bar{2}]_c$.

The XMLD results for LFO on NGO(011)$_o$ and NGO(101)$_o$ are plotted in Figs. 9(a) and 9(b). LFO on NGO is compressively strained along both in-plane directions for either of the two (111)$_{pc}$ facets, but the facets give larger compressive strain along opposite in-plane axes (see Fig. 2). The XMLD signals are weak with a relatively small difference between the $L_{2A/B}$ peaks, consistent with structural domains and in-plane relaxation, as seen from the RSM data, indicating the presence of AF domains. Figure 9(a) shows the data for LFO on NGO(011)$_o$, where the $s$-polarized signal stays constant with $\theta$, while the $p$-polarized signal is significantly reduced for $L_{2B}$ in normal incidence. The more pronounced double peak feature at normal incidence indicates a larger Néel vector alignment for normal incidence than either of the grazing incidence measurements. The $s$-polarized signal indicates a minor component also along the in-plane $[100]_o$. The $p$-polarized signals, comparing the two different grazing incidence scans at 35° and 145°, suggest a small symmetrical out-of-plane component. However, for grazing incidence scans with $\theta = 15°$ and $165°$ (not shown), the out-of-plane component vanishes. Thus, it is inferred that most AF domains in the LFO/NGO(011)$_o$ sample are oriented with in-plane Néel vectors. The data are consistent with a resulting AF order oriented along or close to the $[01\bar{1}]_o$ ($[\bar{1}1\bar{2}]_{pc}$) in-plane principal axis. Considering LFO on NGO(101)$_o$ in Fig. 9(b), the situation is almost identical; the main difference is that the $s$-polarization signal is slightly lower at $L_{2B}$, indicating a somewhat larger proportion of domains aligned along the in-plane $[010]_o$. As for LFO on NGO(011)$_o$, the overall picture is that the average over all AF domains are oriented along or close to the $[10\bar{1}]_o$ ($[11\bar{2}]_{pc}$) in-plane principal axis. Hence, for both NGO(011)$_o$ and NGO(101)$_o$, the inferred average LFO spin axis corresponds to the $\langle 11\bar{2} \rangle_{pc}$ direction, the least $[1.64\%\,\mathrm{NGO}(011)_o]$ and most $[2.00\%\,\mathrm{NGO}(101)_o]$ compressed in-plane axis, respectively. It is noted that when AF domains are present, the inferred spin axis from the XAS data for LFO on NGO does not necessarily reflect the local Néel vector, as the XMLD signal is averaged over many domains due to a beam diameter of $\sim 100\,\mu m$. The rightmost columns of Figs. 9(a) and 9(b) depict both the
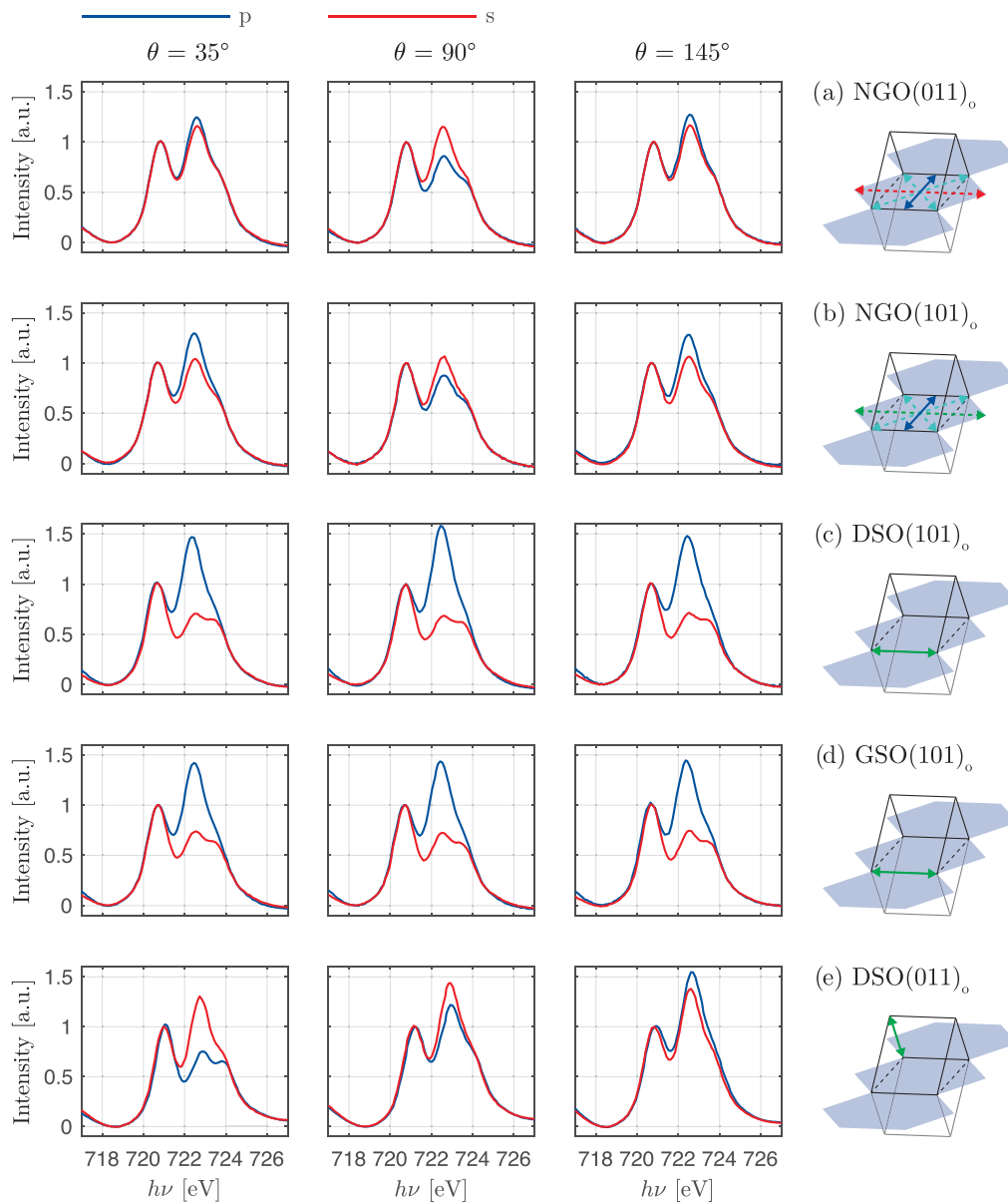
FIG. 9. Fe $L_2$ x-ray absorption spectroscopy (XAS) spectra for *p*- and *s*-polarized x rays normalized at the $L_{2A}$ and $L_2$ pre-edge for LFO on all facets (rows): (a) NGO(011)$_o$, (b) NGO(101)$_o$, (c) DSO(101)$_o$, (d) GSO(101)$_o$, and (e) DSO(011)$_o$. The four columns show from left to right data for increasing x-ray incidence angle and the resulting Néel vector orientation relative to the substrate facets in the rightmost column. Solid arrows indicate the resulting spin axis from the x-ray magnetic linear dichroism (XMLD) data, and dashed arrows indicate possible local Néel vectors in the cases where a monodomain signature was not found. Arrow colors: $a_o$ (red), $b_o$ (green), $\langle 11\bar{2} \rangle_{pc}$ (blue), alternative in-plane $\langle 110 \rangle_{pc}$ axes (turquoise).

direction of the averaged magnetic response (blue arrow), as probed by XMLD spectroscopy, and possible local Néel vectors (dashed arrows) compatible with the inferred structural domains (turquoise and red/green).

The XMLD results for LFO on DSO(101)$_o$ are shown in Fig. 9(c). No significant change in the XAS spectra is seen for any of the three grazing or normal incidence scans. For this situation to occur, the projection of the Néel vector must be the same in all three cases. The *p*-polarized signal has a relative $L_{2B}$ magnitude $> 1.4$ in all cases, indicating more perpendicular alignment, while the *s*-polarization lies $< 0.7$

with a clear double peak for the high energy tail, indicating more parallel alignment. This is consistent with a Néel vector aligned with the in-plane *b* axis [010]$_o$, pointing toward a monodomain AF signature. It is clearly different from LFO on both facets of NGO, and from LFO on STO(111)$_c$, all of which give a polydomain AF response. Similar results were obtained for LFO on GSO(101)$_o$, as shown in Fig. 9(d), with an almost identical XAS response, where the strain conditions and crystal structure are comparable with DSO(101)$_o$. It is noted that the Néel vector direction obtained in these systems, see the rightmost column of Fig. 9 for schematics of the Néel
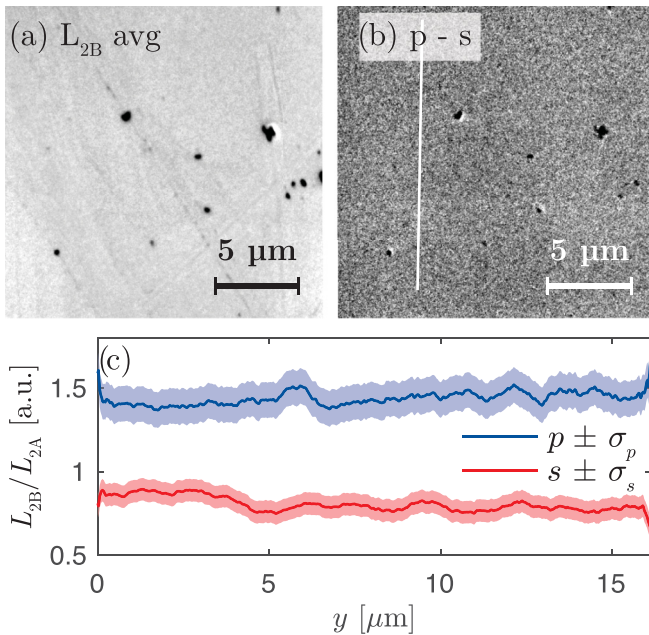
FIG. 10. X-ray magnetic linear dichroism (XMLD) x-ray photoemission electron microscopy (XPEEM) micrographs of the LFO/DSO(101)$_o$ sample showing no sign of antiferromagnetic (AF) domain contrast variation, indicating a magnetic monodomain over the entire field of view ($18.4 \times 18.4 \, \mu m^2$). Images were taken with both $s$- and $p$-polarization, with (a) the average of the $L_{2B}$ peak signal and (b) the XMLD difference image. The black dots and line features seen particularly in (a) are contaminants and scratches due to handling between several different experiments. (c) The renormalized $L_2$ edge data taken along the indicated white line in image (b), showing clear polarization difference consistent with the spectroscopy data.

vectors, coincides with the axis of large tensile strain, the $[\bar{1}10]_{pc}$ direction that is elongated in plane.

To further probe the apparent uniaxial magnetic anisotropy of LFO/DSO(101)$_o$, spatially resolved XMLD maps were taken with XPEEM. Figure 10 shows $L_2$ edge XMLD-XPEEM micrographs with the averaged $L_{2B}$ signals in panel (a) and a uniform magnetic domain contrast in panel (b), consistent with the XMLD spectroscopy data discussed above. In panel (c), the renormalized and smoothed data for the two polarizations along the indicated line in the XMLD micrograph are shown, confirming a clear XMLD signature like the spectroscopy data. The smoothed data are moving averages of the raw data with the standard deviation of the entire line scan plotted in the background for each polarization. Hence, the data indicate either a sample with domains larger than the field of view ($20 \times 20 \, \mu m^2$) or a thin film with macroscopic uniaxial magnetic anisotropy. Literature values for AF domain sizes are typically submicron to a few microns of scale, as reported for LFO [35,37,39], LSFO [58,68], NiO [69,70], CuMnAs [16], and Mn$_2$Au [17], substantially smaller than the field of view in this paper. Hence, consistent with a crystallographic monodomain state from RSM, the XMLD-XPEEM data point toward macroscopic uniaxial anisotropy. It is important to note that 180° AF domains cannot be distinguished in these measurements, as they would result in identical response. Together with the structural data, the XAS

and spatially homogeneous XPEEM data are thus consistent with an AF monodomain state with a uniaxial Néel vector along the in-plane [010]$_o$, the tensile strained direction.

LFO on DSO(011)$_o$ also exhibits a large magnetic anisotropy, as shown in Fig. 9(e). Here, the $s$-polarization signal has increased to $\sim 1.4$ with a minor $\theta$ dependency; however, the $p$-polarization signal is $\theta$ dependent. The low-intensity double peak feature of $L_{2B}$ now occurs distinctively for the $p$-polarized signal at grazing incidence of $\theta = 35°$, consistent with parallel alignment of the x-ray **E** vector, the [010]$_o$ axis, and the AF spin axis. The $p$-polarized $L_{2B}$ peaks gradually increase when the x-ray **E** vector becomes less aligned with the [010]$_o$ axis, first fully in-plane for normal incidence and then out-of-plane almost perpendicular at opposite grazing incidence. This is consistent with a Néel vector along the $b$ axis [010]$_o$, which is pointing out-of-plane at about 55°. The $p$-polarized signal goes from 0.75 to $> 1.5$, indicating a transition from mostly parallel to mostly perpendicular alignment, while the $s$-polarized signal stays $\sim 1.4$ through the series of incidences, indicating little alignment with any spin axis. Thus, the data for LFO on DSO(011)$_o$ are also consistent with a predominantly uniaxial AF state, with the Néel vector along the $[\bar{1}10]_{pc}$ axis that is here elongated out of plane, see the rightmost column of Fig. 9(e). It is noted that the $\theta = 35°$ spectrum can indicate a small contribution also along the in-plane [110]$_{pc}$, as the relative magnitudes are there 0.75 and 1.30 for $p$- and $s$-polarization, respectively. This can be attributed to the larger degree of partial relaxation in the (011)$_o$-oriented film on DSO.

All XMLD results are summarized schematically in the rightmost column of Fig. 9. LFO deposited on DSO(011)$_o$, DSO(101)$_o$, and GSO(101)$_o$ is found to share the same crystallographic Néel vector orientation. Comparing the two (111)$_{pc}$ facets, it is clear that the substrate $b$ axis (green) becomes the preferred spin axis in both cases, out of plane on (011)$_o$ and in plane on (101)$_o$ facets. Interestingly, this is the axis where LFO experiences the largest elongation compared with its bulk structure. Having the Néel vector along the longest of the two primary $a/b$ orthorhombic axes is counterintuitive compared with bulk LFO and the rest of the orthoferrites, where the Néel vector always takes the direction of the shorter $a$ axis [27,29,71]. However, since the AF superexchange mechanism is sensitive to orbital overlap, both energetically and spatially [72,73], small changes in the Fe-O-Fe bond lengths and buckling angles can significantly alter the AF properties [74]. Albeit perovskites are mainly of ionic character, it is noted that the Néel vector is favored by the tensile strain direction in intermetallic manganese-based AF systems where the magnetoelastic coefficient is positive [19]. The results thus suggest that the magnetoelastic coefficient in tensile strained LFO thin films is positive, and the large orthorhombic distortion imposed by the scandate substrates clearly forces the magnetic moments along this direction.

## IV. CONCLUSIONS

By employing large anisotropic strain, structurally monodomain AF thin films are demonstrated. The LFO thin films,

while orthorhombic in bulk, become monoclinic or triclinic depending on the orthorhombic substrate of choice, and the thin films grown on DSO and GSO exhibit a monodomain structure. Magnetically these films show a macroscopic response consistent with a uniaxial Néel vector along the tensile strained pseudo-orthorhombic *b* axis, and no magnetic domains are found. The anisotropic strain also effectively lifts the often-observed degeneracy between the orthorhombic *a* and *b* axes in thin films, supporting a uniaxial AF state. These findings open anisotropic strain as a means to design and engineer AF thin films with a specified Néel vector for spin transport-based applications that minimize the effect of AF domain wall spin resistance. It is anticipated that anisotropic strain engineering can be exploited for designing unique system responses that take advantage of anisotropic phenomena, not necessarily limited to insulating antiferromagnets.

## APPENDIX: DFT CALCULATIONS AND UNIT CELL DATA

The energy landscape for bulk strained LFO was explored by initializing DFT calculations with four different tilt patterns and distortion levels. The results from initializations based on $a^-a^-c^+$ and $a^-a^-c^0$ tilt patterns give similar results for each facet, whereas an $a^-a^-a^-$ initialization gives the same crystal symmetry but different space group. The $a^-a^-c^+$ initialization based on the bulk LFO structure always results in the lowest energy for the strained state, whereas the $a^-a^-c^+$ initialization based on the corresponding substrate facet in some cases come close. All details for the different initializations as well as experimental unit cell data and literature values are tabulated in Table I. Briefly, in general, the lowest energy ground states for bulk strained LFO are found as monoclinic unit cells with $a^-a^-c^+$ Glazer tilt pattern and space group 14, $P2_1/n$ or $P2_1/b$, depending on facet. In some cases, the resulting tilt pattern is changed, see, for example, LFO on NGO(011)$_o$, where the tilt pattern becomes $a^-a^-c^{+(-\delta)}$. A minor out-of-phase rotation $(-\delta)$ is there superimposed on the ordinary in-phase rotations along the long axis, i.e., $c^+ \rightarrow c^{+(-\delta)}$.

Based on the crystal structures calculated by DFT, the unit cell of LFO clearly adopts the in-plane anisotropy of the orthorhombic substrates, see Fig. 11, where the ground state DFT structures ($a^-a^-c^+$ LFO) are visualized. The monoclinic unit cell parameters are plotted in the upper two panels, whereas the two lower panels show the Fe-O-Fe buckling angles and Fe-O bond lengths along pseudocubic
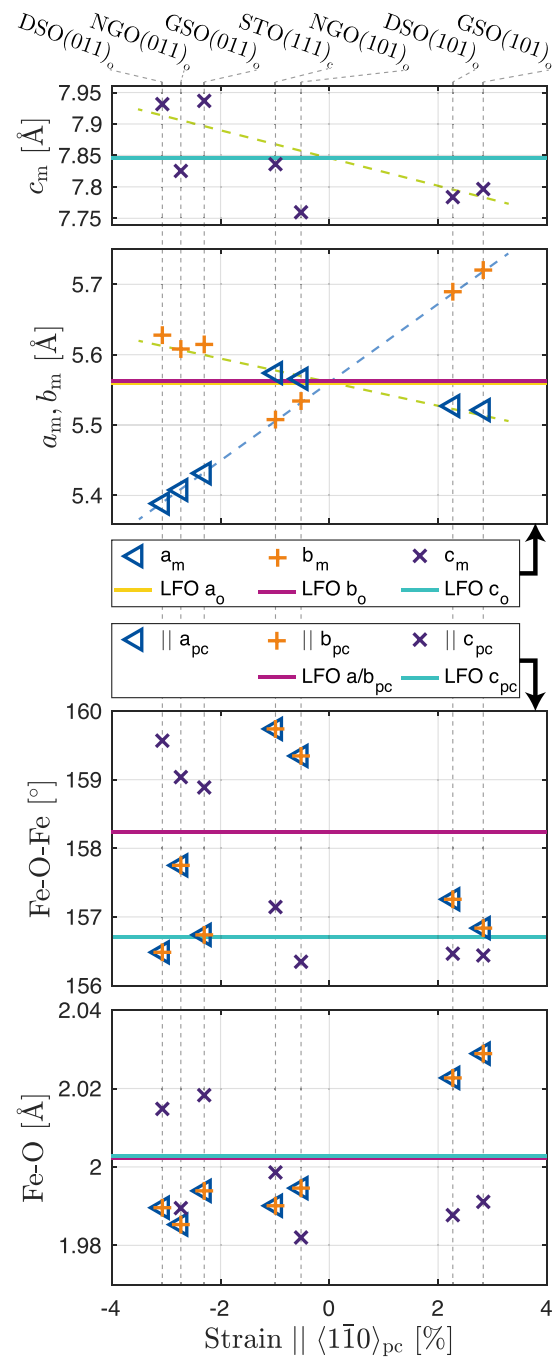


FIG. 11. Visualization of the density functional theory (DFT) data for LFO on all (111)$_{pc}$ facets plotted with respect to the in-plane strain along the *x* axis [$a_o$ for (011)$_o$ and $b_o$ for (101)$_o$ facets]. The monoclinic unit cell parameters are found in the upper two panels. The lower two panels show the Fe-O-Fe buckling angles and Fe-O bond lengths along the respective pseudocubic axes. Solid lines denote the bulk equilibrium values for the orthorhombic LFO found by DFT.

axes. All panels are plotted vs in-plane strain along the $x = \langle 1\bar{1}0 \rangle_{pc}$ direction. The vertical dashed lines denote which data correspond to LFO on each facet referenced on top. The blue dashed line is the linear strain line corresponding to the in-plane $a_o$ and $b_o$ axes for (011)$_o$ and (101)$_o$ facets, respectively. Yellow dashed lines are guides to the eye, showing the

expected response for the out-of-plane axes. It is noted that the experimental RSM data follow the same trends, only with different absolute strain values due to the difference between DFT calculated and experimental lattice parameters. When the substrate distortion is large, as in the scandates (see Fig. 2), the in-phase octahedral rotations increase in amplitude, yielding a reduction of Fe-O-Fe buckling angles along $a_{pc}/b_{pc}$. On the other hand, for LFO on NGO, where the substrate distortion is smaller than for the scandates (see Fig. 2), the in-phase rotations decrease in amplitude, and the buckling angles along $a_{pc}/b_{pc}$ increases. The out-of-phase rotations, represented by the bond angles along $c_{pc}$, seem to depend

mostly on facet, as all $(011)_o$ facets yield increased angles, whereas all $(101)_o$ facets give decreased bond angles and, hence, more buckling. The latter can be directly linked to the deformation settings seen in Figs. 1 and 2, where relative elongation and compression of LFO occur along the in-plane projection of the $c_o$ axis for $(011)_o$ and $(101)_o$, respectively. Following the same trend, all $(011)_o$ facets have longer Fe-O bonds along the $c_{pc}$ axis, and all $(101)_o$ facets have shorter $c_{pc}$ axis bonds. In addition, NGO now has all Fe-O bonds along pseudocubic axes shorter than in bulk LFO, whereas the highly distorted scandates split $a_{pc}/b_{pc}$ and $c_{pc}$ bond lengths above and below bulk LFO values depending on facet.

[1] T. Jungwirth, X. Marti, P. Wadley, and J. Wunderlich, Nat. Nano **11**, 231 (2016).

[2] V. Baltz, A. Manchon, M. Tsoi, T. Moriyama, T. Ono, and Y. Tserkovnyak, Rev. Mod. Phys. **90**, 015005 (2018).

[3] O. Gomonay, V. Baltz, A. Brataas, and Y. Tserkovnyak, Nat. Phys. **14**, 213 (2018).

[4] M. B. Jungfleisch, W. Zhang, and A. Hoffmann, Phys. Lett. A **382**, 865 (2018).

[5] R. Lebrun, A. Ross, S. A. Bender, A. Qaiumzadeh, L. Baldrati, J. Cramer, A. Brataas, R. A. Duine, and M. Kläui, Nature **561**, 222 (2018).

[6] P. Wadley *et al.*, Science **351**, 587 (2016).

[7] K. Olejník, V. Schuler, X. Marti, V. Novák, Z. Kašpar, P. Wadley, R. P. Campion, K. W. Edmonds, B. L. Gallagher, J. Garces, M. Baumgartner, P. Gambardella, and T. Jungwirth, Nat. Commun. **8**, 15434 (2017).

[8] S. Y. Bodnar, L. Šmejkal, I. Turek, T. Jungwirth, O. Gomonay, J. Sinova, A. A. Sapozhnik, H. J. Elmers, M. Kläui, and M. Jourdan, Nat. Commun. **9**, 348 (2018).

[9] M. Meinert, D. Graulich, and T. Matalla-Wagner, Phys. Rev. Appl. **9**, 064040 (2018).

[10] K. Olejník, T. Seifert, Z. Kašpar, V. Novák, P. Wadley, R. P. Campion, M. Baumgartner, P. Gambardella, P. Němec, J. Wunderlich, J. Sinova, P. Kužel, M. Müller, T. Kampfrath, and T. Jungwirth, Sci. Adv. **4**, eaar3566 (2018).

[11] A. Qaiumzadeh, H. Skarsvåg, C. Holmqvist, and A. Brataas, Phys. Rev. Lett. **118**, 137201 (2017).

[12] Z. Qiu, D. Hou, J. Barker, K. Yamamoto, O. Gomonay, and E. Saitoh, Nat. Mater. **17**, 577 (2018).

[13] T. Kosub, M. Kopte, R. Hühne, P. Appel, B. Shields, P. Maletinsky, R. Hübner, M. O. Liedke, J. Fassbender, O. G. Schmidt, and D. Makarov, Nat. Commun. **8**, 13985 (2017).

[14] J.-H. Zheng, A. Brataas, M. Kläui, and A. Qaiumzadeh, Phys. Rev. B **102**, 184413 (2020).

[15] T. Moriyama, K. Oda, T. Ohkochi, M. Kimata, and T. Ono, Sci. Rep. **8**, 14167 (2018).

[16] M. J. Grzybowski, P. Wadley, K. W. Edmonds, R. Beardsley, V. Hills, R. P. Campion, B. L. Gallagher, J. S. Chauhan, V. Novak, T. Jungwirth, F. Maccherozzi, and S. S. Dhesi, Phys. Rev. Lett. **118**, 057701 (2017).

[17] A. A. Sapozhnik, M. Filianina, S. Y. Bodnar, A. Lamirand, M. A. Mawass, Y. Skourski, H. J. Elmers, H. Zabel, M. Kläui, and M. Jourdan, Phys. Rev. B **97**, 134429 (2018).

[18] D. G. Schlom, L.-Q. Chen, C. J. Fennie, V. Gopalan, D. A. Muller, X. Pan, R. Ramesh, and R. Uecker, MRS Bull. **39**, 118 (2014).

[19] I. J. Park, T. Lee, P. Das, B. Debnath, G. P. Carman, and R. K. Lake, Appl. Phys. Lett. **114**, 142403 (2019).

[20] H. Yan, Z. Feng, S. Shang, X. Wang, Z. Hu, J. Wang, Z. Zhu, H. Wang, Z. Chen, H. Hua, W. Lu, J. Wang, P. Qin, H. Guo, X. Zhou, Z. Leng, Z. Liu, C. Jiang, M. Coey, and Z. Liu, Nat. Nanotechnol. **14**, 131 (2019).

[21] N. Waterfield Price, A. M. Vibhakar, R. D. Johnson, J. Schad, W. Saenrang, A. Bombardi, F. P. Chmiel, C. B. Eom, and P. G. Radaelli, Phys. Rev. Appl. **11**, 024035 (2019).

[22] J. R. Kim, J. Jang, K.-J. Go, S. Y. Park, C. J. Roh, J. Bonini, J. Kim, H. G. Lee, K. M. Rabe, J. S. Lee, S.-Y. Choi, T. W. Noh, and D. Lee, Nat. Commun. **11**, 4944 (2020).

[23] J. Park, Y. Kim, D. Lee, J. H. Song, and J.-H. Park, J. Korean Phys. Soc. **76**, 273 (2020).

[24] S. Geller, J. Chem. Phys. **24**, 1236 (1956).

[25] S. Geller and E. A. Wood, Acta Crystallogr. **9**, 563 (1956).

[26] W. C. Koehler and E. O. Wollan, J. Phys. Chem. Solids **2**, 100 (1957).

[27] W. C. Koehler, E. O. Wollan, and M. K. Wilkinson, Phys. Rev. **118**, 58 (1960).

[28] D. Treves, J. Appl. Phys. **36**, 1033 (1965).

[29] R. L. White, J. Appl. Phys. **40**, 1061 (1969).

[30] S. Geller and P. M. Raccah, Phys. Rev. B **2**, 1167 (1970).

[31] S. M. Selbach, J. R. Tolchard, A. Fossdal, and T. Grande, J. Solid State Chem. **196**, 249 (2012).

[32] M. Marezio and P. D. Dernier, Mater. Res. Bull. **6**, 23 (1971).

[33] S. C. Abrahams, R. L. Barns, and J. L. Bernstein, Solid State Commun. **10**, 379 (1972).

[34] A. Fossdal, M. A. Einarsrud, and T. Grande, J. Eur. Ceram. Soc. **25**, 927 (2005).

[35] A. Scholl, J. Stöhr, J. Lüning, J. W. Seo, J. Fompeyrine, H. Siegwart, J.-P. Locquet, F. Nolting, S. Anders, E. E. Fullerton, M. R. Scheinfein, and H. A. Padmore, Science **287**, 1014 (2000).

[36] F. Nolting, A. Scholl, J. Stöhr, J. W. Seo, J. Fompeyrine, H. Siegwart, J. P. Locquet, S. Anders, J. Lüning, E. E. Fullerton, M. F. Toney, M. R. Scheinfein, and H. A. Padmore, Nature **405**, 767 (2000).

[37] J. Lüning, F. Nolting, A. Scholl, H. Ohldag, J. W. Seo, J. Fompeyrine, J. P. Locquet, and J. Stöhr, Phys. Rev. B **67**, 214433 (2003).

[38] J. W. Seo, E. E. Fullerton, F. Nolting, A. Scholl, J. Fompeyrine, and J. P. Locquet, J. Phys. Condens. Matter **20**, 264014 (2008).

[39] I. Hallsteinsen, M. Moreau, R. V. Chopdekar, E. Christiansen, M. Nord, P. E. Vullum, J. K. Grepstad, R. Holmestad, S. M. Selbach, A. Scholl, E. Arenholz, E. Folven, and T. Tybell, APL Materials **5**, 086107 (2017).

[40] I. Hallsteinsen, M. Nord, T. Bolstad, P.-E. Vullum, J. E. Boschker, P. Longo, R. Takahashi, R. Holmestad, M. Lippmaa, and T. Tybell, Cryst. Growth Des. **16**, 2357 (2016).

[41] R. P. Liferovich and R. H. Mitchell, J. Solid State Chem. **177**, 2188 (2004).

[42] W. Marti, P. Fischer, J. Schefer, and F. Kubel, Z. Kristallogr. Cryst. Mater. **211**, 891 (1996).

[43] A. A. Levin, P. Paufler, and D. C. Meyer, Physica B **393**, 373 (2007).

[44] A. Glazer, Acta Cryst. **28**, 3384 (1972).

[45] K. Momma and F. Izumi, J. Appl. Crystallogr. **44**, 1272 (2011).

[46] K. Kjærnes, T. Bolstad, D. M. Evans, E. Lysne, B. A. D. Williamson, D. Meier, S. M. Selbach, and T. Tybell, arXiv:2011.12874 (2020).

[47] G. Kresse and J. Furthmüller, Phys. Rev. B **54**, 11169 (1996).

[48] G. Kresse and D. Joubert, Phys. Rev. B **59**, 1758 (1999).

[49] P. E. Blöchl, Phys. Rev. B **50**, 17953 (1994).

[50] J. P. Perdew, A. Ruzsinszky, G. I. Csonka, O. A. Vydrov, G. E. Scuseria, L. A. Constantin, X. Zhou, and K. Burke, Phys. Rev. Lett. **100**, 136406 (2008).

[51] S. L. Dudarev, G. A. Botton, S. Y. Savrasov, C. J. Humphreys, and A. P. Sutton, Phys. Rev. B **57**, 1505 (1998).

[52] I. Hallsteinsen, M. Moreau, A. Grutter, M. Nord, P. E. Vullum, D. A. Gilbert, T. Bolstad, J. K. Grepstad, R. Holmestad, S. M. Selbach, A. T. N'Diaye, B. J. Kirby, E. Arenholz, and T. Tybell, Phys. Rev. B **94**, 201115(R) (2016).

[53] R. L. Johnson-Wilke, D. Marincel, S. Zhu, M. P. Warusawithana, A. Hatt, J. Sayre, K. T. Delaney, R. Engel-Herbert, C. M. Schlepütz, J. W. Kim, V. Gopalan, N. A. Spaldin, D. G. Schlom, P. J. Ryan, and S. Trolier-McKinstry, Phys. Rev. B **88**, 174101 (2013).

[54] M. Moreau, A. Marthinsen, S. M. Selbach, and T. Tybell, Phys. Rev. B **96**, 094109 (2017).

[55] I. Hallsteinsen, A. Grutter, M. Moreau, S. D. Slöetjes, K. Kjærnes, E. Arenholz, and T. Tybell, Phys. Rev. Materials **2**, 084403 (2018).

[56] Y. Jia, R. V. Chopdekar, P. Shafer, E. Arenholz, Z. Liu, M. D. Biegalski, and Y. Takamura, Phys. Rev. B **96**, 214411 (2017).

[57] Y. Jia, R. V. Chopdekar, E. Arenholz, Z. Liu, M. D. Biegalski, Z. D. Porter, A. Mehta, and Y. Takamura, Phys. Rev. B **93**, 104403 (2016).

[58] Y. Jia, R. V. Chopdekar, E. Arenholz, A. T. Young, M. A. Marcus, A. Mehta, and Y. Takamura, Phys. Rev. B **92**, 094407 (2015).

[59] S. Czekaj, F. Nolting, L. J. Heyderman, P. R. Willmott, and G. van der Laan, Phys. Rev. B **73**, 020401(R) (2006).

[60] E. Arenholz, G. van der Laan, F. Yang, N. Kemik, M. D. Biegalski, H. M. Christen, and Y. Takamura, Appl. Phys. Lett. **94**, 072503 (2009).

[61] E. Arenholz, G. van der Laan, R. V. Chopdekar, and Y. Suzuki, Phys. Rev. B **74**, 094407 (2006).

[62] G. van der Laan and B. T. Thole, Phys. Rev. B **43**, 13401 (1991).

[63] G. van der Laan, E. Arenholz, R. V. Chopdekar, and Y. Suzuki, Phys. Rev. B **77**, 064407 (2008).

[64] H. T. Stokes and D. M. Hatch, J. Appl. Crystallogr. **38**, 237 (2005).

[65] FINDSYM, ISOTROPY Software Suite, https://iso.byu.edu/iso/isotropy.php (2020).

[66] E. Christiansen, M. Nord, I. Hallsteinsen, P. E. Vullum, T. Tybell, and R. Holmestad, J. Phys. Conf. Ser. **644**, 012002 (2015).

[67] M. Nord, A. Ross, D. McGrouther, J. Barthel, M. Moreau, I. Hallsteinsen, T. Tybell, and I. MacLaren, Phys. Rev. Materials **3**, 063605 (2019).

[68] M. S. Lee, P. Lyu, R. V. Chopdekar, A. Scholl, S. T. Retterer, and Y. Takamura, J. Appl. Phys. **127**, 203901 (2020).

[69] J. Stöhr, A. Scholl, T. J. Regan, S. Anders, J. Lüning, M. R. Scheinfein, H. A. Padmore, and R. L. White, Phys. Rev. Lett. **83**, 1862 (1999).

[70] H. Ohldag, A. Scholl, F. Nolting, S. Anders, F. U. Hillebrecht, and J. Stöhr, Phys. Rev. Lett. **86**, 2878 (2001).

[71] T. Peterlin-Neumaier and E. Steichele, J. Magn. Magn. Mater. **59**, 351 (1986).

[72] J. B. Goodenough, Phys. Rev. **100**, 564 (1955).

[73] J. Kanamori, J. Phys. Chem. Solids **10**, 87 (1959).

[74] H. Weihe and H. U. Güdel, Inorg. Chem. **36**, 3632 (1997).